



Photocatalytic ammonia synthesis from nitrate reduction on nickel single-atom decorated on defective tungsten oxide



Yunlong Wang ^{a,b,1}, Haibo Yin ^{b,1,*}, Xiaoguang Zhao ^{a,1}, Yakun Qu ^a, Aiguo Zheng ^a, Han Zhou ^a, Wei Fang ^{a,*}, Junhua Li ^{b,*}

^a Sinopec Research Institute of Petroleum Processing Co., Ltd, Beijing 100083, PR China

^b State Key Joint Laboratory of Environment Simulation and Pollution Control, School of Environment, Tsinghua University, Beijing 100084, PR China

ARTICLE INFO

Keywords:
Photocatalytic NH₃ synthesis
NO₃ reduction
Single-atom
Oxygen vacancies
Orbital hybridizations

ABSTRACT

Photocatalytic reduction of waste nitrate (NO₃) into value-added ammonia (NH₃) under ambient conditions has enormous advantages over the Haber-Bosch process. However, weak adsorption capacity and low efficiency of photocatalysts limit its large-scale application. Here, Ni single-atom (SA) on defective WO₃ (Ni/H_xWO_{3-y}) hybrids with abundant oxygen vacancies (OVs) are synthesized by a facile H-spillover process, which exhibits a high NH₃ rate of 10.5 mmol g⁻¹ h⁻¹ and 98.26 % NH₃ selectivity. In situ characterizations and theoretical calculations demonstrate the activity mainly derives from the synergistic effect of OVs and Ni SAs. That is, (1) photogenerated electrons and adsorbed NO₃ transfer from OVs to Ni SAs; (2) the strong hybridizations of Ni 3d - O 2p orbitals of NO₃ accelerate electron transfer from Ni SAs to NO₃; (3) Ni SAs effectively reduce the free energy of the rate-limiting step (NO₂^{*} → NO^{*}) of H_xWO_{3-y}. In simulated wastewater, the durable performance of Ni/H_xWO_{3-y} hybrids proves great potential in industrial applications.

1. Introduction

Ammonia (NH₃) is regarded as an essential chemical and a potential carrier of hydrogen energy [1–3]. Currently, industrial-scale NH₃ synthesis relies heavily on the Haber-Bosch process requiring severe operating conditions of high temperatures and pressures [4,5]. Additionally, nitrate (NO₃) pollutants in nature pose a serious danger to human health [6]. Although several industrial strategies for treating NO₃ wastewater have been adopted, such as ion exchange and microbial transformation, their practical applicability is restricted by their expensive cost and/or complicated processes [7,8]. Hence, the promising strategy for photocatalytic NH₃ synthesis from NO₃ reduction at ambient conditions has attracted much attention recently due to the advantages of sustainability, cleanliness, and low energy consumption [1,9–12]. Moreover, it should be noted that some organic substances, such as alcohols and aldehydes, which can serve as hole scavengers in the photocatalytic process, are also widely dispersed in NO₃-containing wastewater [9,12]. Therefore, photocatalytic synergistic reduction of NO₃ for NH₃ synthesis and removal of organic matter is of great importance for the treatment of water pollution and development of sustainable energy economy.

However, weak adsorption capacity for NO₃ and low efficiency for NH₃ synthesis of photocatalysts limit their large-scale application [13].

To increase efficient active sites and improve carrier separation efficiency of catalysts on photocatalytic NO₃ reduction [14,15], many effective strategies, such as defect structure construction [16], cocatalyst loading [17], and band gap engineering [18], have been proposed to obtain highly selective products [19]. Notably, constructing oxygen vacancies (OVs) on semiconductor surfaces is an effective method for enhancing photocatalytic activity [20]. The localized surface plasmon resonance (LSPR) of transition metal oxides with plenty of OVs is capable of inducing a large number of localized electrons and has been shown to be very effective in the adsorption and activation of small molecules such as N₂ [21,22] and CO₂ [23,24]. Yamashita's group reported that abundant localized electrons induced by sustained OVs on 2D H_xMoO_{3-y} nanosheets can greatly promote charge-carrier separation in the visible region [25], ultimately improving photocurrent responsiveness and photocatalytic activity. As another n-type semiconductor, tungsten trioxide (WO₃) has a wide bandgap (2.8 eV) [26]. The heavily doped non-stoichiometric counterpart (H_xWO_{3-y}) with abundant OVs has an extensive solar absorption region induced by LSPRs, which can

* Corresponding authors.

E-mail addresses: yinhalbqifei@tsinghua.edu.cn (H. Yin), fangwei.ripp@sinopec.com (W. Fang), lijunhua@tsinghua.edu.cn (J. Li).

¹ These authors contributed equally to this work.

effectively adsorb and activate NO_3^- . On the other hand, compared with metal nanoparticles (NPs), single-atom (SA) catalysts exhibit effective catalytic activity and provide an atomic-scale perspective of understanding the reaction mechanism, which have ultra-high atom utilization and unique electronic structure [27–30]. Moreover, due to the unique spatial isolation property, the monoatomic active site can effectively avoid N^*-N^* coupling required for N_2 and N_2O [31–33]. Currently, it has been reported that non-noble metal Ni SA plays an important role in binding H^* [34] and has a strong adsorption effect on important intermediates such as NO_2^* and NH_2^* [35,36]. Therefore, considering the advantages of OVs and SAs in NO_3^- reduction to NH_3 , it is significant and necessary to obtain Ni SAs decorated on plasmonic $\text{H}_x\text{WO}_{3-y}$ (denoted as $\text{Ni}/\text{H}_x\text{WO}_{3-y}$), which are expected to show synergistic multilevel coupling effects for further improving NH_3 synthesis efficiency.

In this work, we report Ni SAs decorated on heavily hydrogen-doped WO_3 ($\text{Ni}/\text{H}_x\text{WO}_{3-y}$) hybrids by a facile H-spillover route. $\text{Ni}/\text{H}_x\text{WO}_{3-y}$ hybrids with abundant OVs exhibit strong visible light absorption with the LSPR peak at around 550 nm, which greatly improves the utilization of full-spectrum light. Relative to pristine WO_3 , $\text{Ni}/\text{H}_x\text{WO}_{3-y}$ hybrids with dual active sites of OVs and Ni SAs effectively promote photocatalytic NO_3^- reduction under ambient conditions with NH_3 yield of 10.5 mmol $\text{g}_{\text{cat}}^{-1} \text{ h}^{-1}$ and 98.26 % NH_3 selectivity in a certain leading position in the area of NH_3 synthesis. More importantly, in situ electron paramagnetic resonance (EPR), in situ diffused reflectance infrared Fourier transform spectroscopy (DRIFT), and density generalized function theory (DFT) calculations successfully reveal the reaction mechanism and the origin of high activity of $\text{Ni}/\text{H}_x\text{WO}_{3-y}$ hybrids. In addition, the simulation application of $\text{Ni}/\text{H}_x\text{WO}_{3-y}$ hybrids in real polluted water bodies provide a promising strategy with industrial development prospects.

2. Experimental section

2.1. Synthesis of $\text{Ni}/\text{H}_x\text{WO}_{3-y}$ hybrids

In a typical synthesis, 400 mg of commercial WO_3 was dispersed in 50 mL of aqueous solution. Subsequently, 35 mg of polyvinylpyrrolidone K-30 (PVP) and an amount of NiCl_2 solution were injected into the reaction solution and stirred for 6 h under magnetic stirring. The Ni percentage was maintained at 0.5 wt%. Finally, the powder (Ni/WO_3) was calcined in a tube furnace at 500 °C for 3 h under hydrogen atmosphere.

2.2. Material characterization

The samples were characterized by various measurements, including X-ray diffraction (XRD), X-ray photoelectron spectroscopy (XPS), Raman, nitrogen adsorption, scanning electron microscopy (SEM), transmission electron microscopy (TEM), energy-dispersive spectroscopy (EDS), X-ray absorption fine structure (XAFS), ^1H nuclear magnetic resonance (^1H NMR), UV/Vis-NIR diffuse reflectance, photocurrent response, impedance curves, Mott-Schottky curves, PL spectra, time-resolved fluorescence decay spectra, Fourier-transform infrared spectra (FT-IR), electron paramagnetic resonance (EPR), in situ diffuse reflectance infrared Fourier transform spectroscopy (in situ DRIFTS), and in situ electron paramagnetic resonance (in situ EPR). The detailed operation procedures of the above characterizations can be found in [Supporting Information](#).

2.3. Catalytic performance measurements

The catalytic test procedures including catalytic activities for photocatalytic NO_3^- reduction, apparent quantum efficiency (AQE), and long-term stability are shown in [Supporting Information](#) in detail.

2.4. DFT calculation detail

The density functional theory (DFT) calculations were conducted with the Vienna ab initio simulation package (VASP). The model structures were optimized using the Perdew-Burke-Ernzerhof (PBE) form of the generalized gradient approximation plus the Hubbard model (GGA), with 400 eV of kinetic cutoff energy and a k-point mesh of $2 \times 2 \times 1$ in Monkhorst-Pack scheme. The computational hydrogen electrode method was applied to calculate the adsorption free energies. More details of computational methods can be found in [Supporting Information](#).

3. Results and discussion

3.1. Structure and morphology of $\text{Ni}/\text{H}_x\text{WO}_{3-y}$ hybrids

Fig. 1a displays the synthetic process of Ni SAs decorated on heavily hydrogen-doped WO_3 by a facile H-spillover process. The in-situ formed Ni SAs cause a rapid dissociation of H_2 to dopants ($^*\text{H}$). Then, free electrons and $^*\text{H}$ migrate to WO_3 , which leads to the partial reduction of W^{6+} [22,37]. The scanning electron microscopy (SEM) images (**Fig. S1**) show that $\text{Ni}/\text{H}_x\text{WO}_{3-y}$ hybrids and reference samples (WO_3 , Ni/WO_3 , and $\text{H}_x\text{WO}_{3-y}$) maintain rod-like structures of WO_3 . The high-angle annular dark-field scanning transmission electron microscope (HAADF-STEM) image (**Fig. 1b**) of $\text{Ni}/\text{H}_x\text{WO}_{3-y}$ hybrids exhibits that no Ni NPs but only isolated Ni SAs labeled with white circles are clearly observed on $\text{H}_x\text{WO}_{3-y}$. Energy dispersive X-ray (EDX) spectrometry (**Fig. 1c**) show that W, O, and Ni elements are uniformly distributed on $\text{Ni}/\text{H}_x\text{WO}_{3-y}$ hybrids. The high-resolution transmission electron microscopy (HRTEM) image of the $\text{Ni}/\text{H}_x\text{WO}_{3-y}$ hybrids (**Fig. 1d**) indicates clear lattice fringes with interplanar spacings of 0.364 nm, corresponding to the (200) plane of WO_3 . Notably, a disordered surface layer with a thickness of about 1 nm can be observed in $\text{Ni}/\text{H}_x\text{WO}_{3-y}$ hybrids (**Fig. S2**), which mainly stems from the introduction of OVs during H-spillover process [38–40]. The adsorption-desorption of N_2 analysis (**Fig. S3**) show that $\text{Ni}/\text{H}_x\text{WO}_{3-y}$ hybrids and reference samples exhibit similar mesopore diameter distribution (2.07 nm), pore volume (0.0054 $\text{cm}^3 \text{ g}^{-1}$), and Brunauer-Emmett-Teller (BET) surface area (0.9839 $\text{m}^2 \text{ g}^{-1}$), indicating both Ni SAs and OVs have no significant effect on the structure of catalysts.

From the powder X-ray diffraction (XRD) patterns of $\text{Ni}/\text{H}_x\text{WO}_{3-y}$ hybrids (**Fig. 1e**) and reference samples (**Fig. S4a**), the peaks at 23.1, 23.6, and 24.4° are ascribed to the (002), (020), and (200) crystal planes of monoclinic WO_3 (PDF#83-0950) [41,42]. Meanwhile, it is visible that the above diffraction peaks of $\text{H}_x\text{WO}_{3-y}$ and $\text{Ni}/\text{H}_x\text{WO}_{3-y}$ hybrids (**Fig. S4b**) are slightly biased toward lower diffraction angles compared to those of pristine WO_3 and Ni/WO_3 , suggesting the distortion and expansion of the lattice after H-spillover process [40]. Furthermore, compared to pristine WO_3 and Ni/WO_3 , the three main vibrational bands at 711.5, 262.7, and 800.0 cm^{-1} in Raman spectra (**Fig. S5**) of $\text{H}_x\text{WO}_{3-y}$ and $\text{Ni}/\text{H}_x\text{WO}_{3-y}$ hybrids belong to bending vibration of $\delta(\text{O}-\text{W}-\text{O})$, stretching vibration of $\nu(\text{W}-\text{O}-\text{W})$ and W-O stretching of the monoclinic phase, respectively, where OVs leads to peaks shift to lower wavelengths [37,43,44]. Furthermore, according to the Fourier transform infrared (FTIR) spectra (**Fig. S6**), the absorption peaks of 1041 cm^{-1} , 795 cm^{-1} , and 584 cm^{-1} can be assigned to the W-O, O-W-O, and W-O-W bonds, respectively [45,46]. The above absorption peaks in $\text{Ni}/\text{H}_x\text{WO}_{3-y}$ hybrids are broader compared to those of WO_3 , indicating that the introduction of more OVs in $\text{Ni}/\text{H}_x\text{WO}_{3-y}$ hybrids results in the weaker vibrations of the above bonds [47,48]. According to the UV/Vis-NIR spectra (**Fig. 1f** and **Fig. S7a**), $\text{H}_x\text{WO}_{3-y}$ and $\text{Ni}/\text{H}_x\text{WO}_{3-y}$ hybrids show strong light responses in the visible and near-infrared regions, especially $\text{Ni}/\text{H}_x\text{WO}_{3-y}$ hybrids which have a strong LSPR peak pinning at around 550 nm. In contrast, WO_3 and Ni/WO_3 only exhibit similar intrinsic absorption below about 480 nm [26,37], which is attributed to the indirect bandgap absorption edge of WO_3 (around

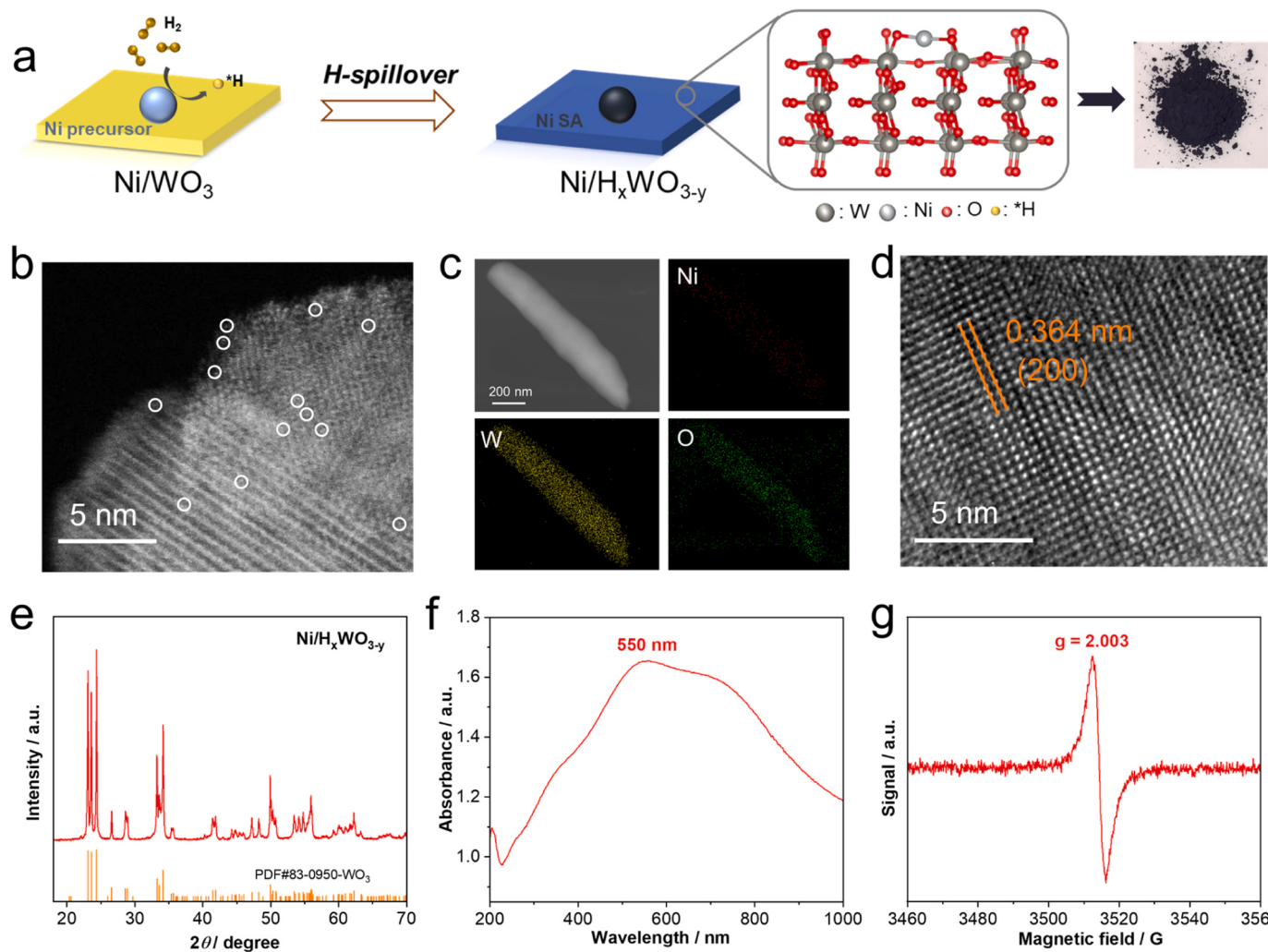


Fig. 1. (a) Schematic diagram of the synthetic process, (b) HRTEM image, (c) EDX elemental mappings, (d) high-resolution HAADF-STEM image, (e) XRD pattern, (f) UV/Vis-NIR absorption spectrum, and (g) EPR spectrum of $\text{Ni}/\text{H}_x\text{WO}_{3-y}$ hybrids.

2.8 eV)¹⁰. EPR spectroscopy is performed to further examine the surface OVs (Fig. 1g and Fig. S8). The g value in WO_3 shows a weak peak at 2.003 from the single electron trapped by OVs. $\text{Ni}/\text{H}_x\text{WO}_{3-y}$ hybrids show the highest peak compared to references, demonstrating a significant increase in OVs concentration in $\text{Ni}/\text{H}_x\text{WO}_{3-y}$ hybrids.

In addition, other metal SAs decorated on $\text{H}_x\text{WO}_{3-y}$ including the noble metal $\text{Pd}/\text{H}_x\text{WO}_{3-y}$ hybrids (Fig. S9) and the transition metal $\text{Cu}/\text{H}_x\text{WO}_{3-y}$ hybrids (Fig. S10) are prepared by the same H-spillover process. Detailed characterizations confirm the uniform distribution of metal SAs and the formation of OVs on $\text{H}_x\text{WO}_{3-y}$ supports. Moreover, both $\text{Pd}/\text{H}_x\text{WO}_{3-y}$ hybrids and $\text{Cu}/\text{H}_x\text{WO}_{3-y}$ hybrids have similar structure (Fig. S5b) and light absorption ability (Fig. S7b) as $\text{Ni}/\text{H}_x\text{WO}_{3-y}$ hybrids.

3.2. Structural parameters and coordination environment

To explore the fine chemical composition and atomic-level structure of $\text{Ni}/\text{H}_x\text{WO}_{3-y}$ hybrids, we perform X-ray photoelectron spectroscopy (XPS) and X-ray absorption fine structure (XAFS) analysis. Based on the O 1 s XPS spectra (Fig. S11), the peak at 530.65 eV is attributed to lattice oxygen ($\text{O}_{\text{latt.}}$) in $\text{Ni}/\text{H}_x\text{WO}_{3-y}$ hybrids, whereas other peaks at 531.85 and 532.95 eV are assigned to -OH groups (O_{OH}) and -OH₂ groups (O_{H2O}), respectively. Compared to WO_3 and Ni/WO_3 , the peak intensities of O_{OH} species in $\text{Ni}/\text{H}_x\text{WO}_{3-y}$ hybrids and $\text{H}_x\text{WO}_{3-y}$ significantly enhance after H-spillover process, demonstrating the formation of

W-OH bond. The enhanced W-OH bond concentration after H intercalation absolutely matches the analysis results of Raman and EPR spectra. Furthermore, no Ni^0 peaks can be found in the Ni 2p XPS of $\text{Ni}/\text{H}_x\text{WO}_{3-y}$ hybrids (Fig. S12), suggesting Ni species exist in the form of Ni-O coordination rather than Ni NPs. From W 4f XPS spectra (Fig. S13) of $\text{Ni}/\text{H}_x\text{WO}_{3-y}$ hybrids, the peaks at 35.95 and 38.05 eV are attributed to the major W species (W^{6+}), while the appearance of the low oxidation state W^{5+} is also observed (34.65 and 36.85 eV). In contrast, only W^{6+} species are present in pristine WO_3 , suggesting the partial reduction of W^{6+} during H-spillover process. The calculation of the XPS peak area of W 4f shows that W^{6+} and W^{5+} account for 86 % and 14 % of the total W elements, respectively. The average oxidation state of W species in $\text{Ni}/\text{H}_x\text{WO}_{3-y}$ hybrids is further calculated to be 5.86, which arises from the OVs. Moreover, peaks position of both O 1 s and W 4f in $\text{Ni}/\text{H}_x\text{WO}_{3-y}$ hybrids change to higher binding energies compared to WO_3 , demonstrating that the electron transfers from the $\text{H}_x\text{WO}_{3-y}$ to Ni SAs, making Ni species in incomplete oxidation state.

To further determine chemical state and atomic coordination structures of Ni and W species in $\text{Ni}/\text{H}_x\text{WO}_{3-y}$ hybrids, the XAFS spectra of $\text{Ni}/\text{H}_x\text{WO}_{3-y}$ hybrids and references are acquired at Ni K-edge and W L₃-edge, respectively. According to X-ray near-edge structure (XANES) spectroscopy (Fig. 2a), the peak location of $\text{Ni}/\text{H}_x\text{WO}_{3-y}$ hybrids (red line, 8350.0 eV) shifts to higher energy compared to Ni foil (gray line, 8350.7 eV), proving that Ni SAs in $\text{Ni}/\text{H}_x\text{WO}_{3-y}$ hybrids exhibit electron-deficient features. Moreover, the absorption edge of Ni/

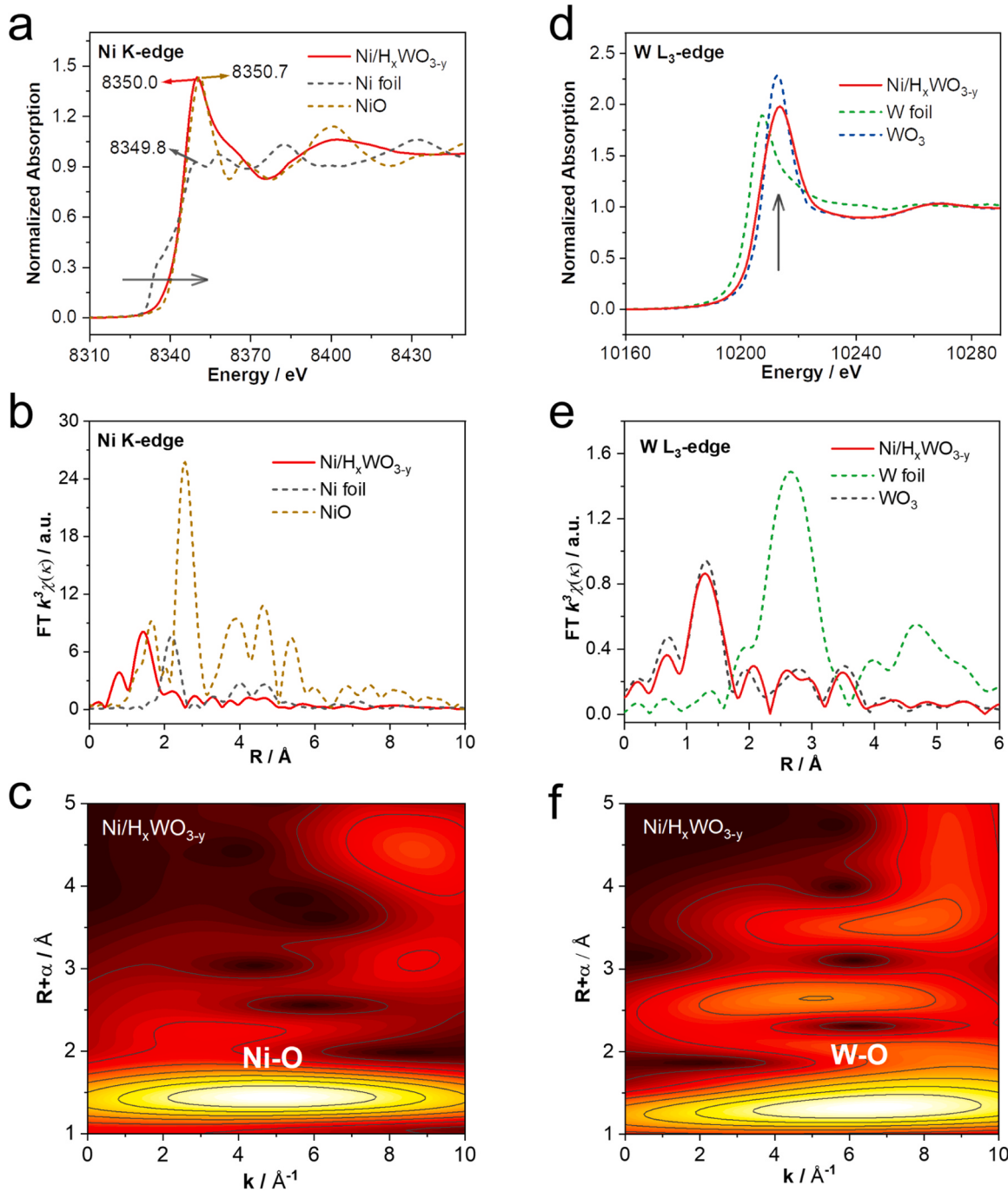


Fig. 2. (a) XANES spectra, (b) FT-EXAFS spectra, and (c) WT-EXAFS spectra at Ni K-edge of $\text{Ni}/\text{H}_x\text{WO}_{3-y}$ hybrids and references. (d) XANES spectra, (e) FT-EXAFS spectra, and (f) WT-EXAFS spectra at W L_3 -edge of $\text{Ni}/\text{H}_x\text{WO}_{3-y}$ hybrids and references.

$\text{H}_x\text{WO}_{3-y}$ hybrids is between NiO (brown line) and Ni foil (black arrow), indicating that the valence state of Ni SAs ranges from 0 to + 2. From the Fourier transformation EXAFS (FT-EXAFS) curves (Fig. 2b) of $\text{Ni}/\text{H}_x\text{WO}_{3-y}$ hybrids and references, the lengths of Ni-O bond and Ni-Ni bond are 1.66 Å and 2.18 Å, respectively. No Ni-Ni bonds are found in $\text{Ni}/\text{H}_x\text{WO}_{3-y}$ hybrids, proving that Ni atoms are atomically dispersed and coordinated with O atoms (1.45 Å) in $\text{Ni}/\text{H}_x\text{WO}_{3-y}$ hybrids. This corresponds to the analysis of HADDF-STEM images (Fig. 1b). Wavelet transform (WT)-EXAFS oscillations are carried out in both K and R spaces in order to better observe the atomic conformation of Ni species over $\text{Ni}/\text{H}_x\text{WO}_{3-y}$ hybrids. The WT-EXAFS contour plot of $\text{Ni}/\text{H}_x\text{WO}_{3-y}$ hybrids (Fig. 2c) reveals Ni-O coordination through a maximum of around 1.45 Å. No typical Ni NPs (Fig. S14a; 2.18 Å) and NiO (Fig. S14b;

2.60 Å) signals are observed in $\text{Ni}/\text{H}_x\text{WO}_{3-y}$ hybrids. In addition, the O coordination mode of Ni species in $\text{Ni}/\text{H}_x\text{WO}_{3-y}$ hybrids is also further determined by Ni K-edge EXAFS fitting analysis (Fig. S14c-d and Table S1). Furthermore, W L_3 -edge XANES spectra (Fig. 2d) show that W peak intensity (red line) lies between WO_3 (blue line) and W foil (green line), reflecting that the valence range of W species in $\text{Ni}/\text{H}_x\text{WO}_{3-y}$ hybrids is between 0 and + 6. It can be observed from the FT-EXAFS curves (Fig. 2e) that the intensity of the first shell layer coordination peak of $\text{Ni}/\text{H}_x\text{WO}_{3-y}$ hybrids decreases and shifts 0.03 Å toward the lower R, which is attributed to the local atomic alignment change [49]. The abundant OVs reduce the coordination number of W species in $\text{Ni}/\text{H}_x\text{WO}_{3-y}$ hybrids and shorten the exposed W-O bond length to enhance electron transfer [50]. Furthermore, the coordination mode and

bonds length (1.32 Å) of W in $\text{Ni}/\text{H}_x\text{WO}_{3-y}$ hybrids are also determined by WT-EXAFS oscillations (Fig. 2f and Fig. S15a-b) and W L₃-edge EXAFS fitting analysis (Fig. S15c-d and Table S2). Similarly, the XAFS spectra of $\text{Pd}/\text{H}_x\text{WO}_{3-y}$ hybrids (Fig. S16, Fig. S17, Table S2, and Table S3) and $\text{Cu}/\text{H}_x\text{WO}_{3-y}$ hybrids (Fig. S18 and Table S4) indicate that the configurations of metal SAs and OVs are also successfully obtained in $\text{Pd}/\text{H}_x\text{WO}_{3-y}$ hybrids and $\text{Cu}/\text{H}_x\text{WO}_{3-y}$ hybrids.

3.3. The charge carrier dynamics and band structures of $\text{Ni}/\text{H}_x\text{WO}_{3-y}$ hybrids

To elucidate the roles of Ni SAs coupled OVs in enhancing photo-generated electron dynamics, the photochemical properties and photoluminescence spectra of $\text{Ni}/\text{H}_x\text{WO}_{3-y}$ hybrids and reference samples are investigated. $\text{Ni}/\text{H}_x\text{WO}_{3-y}$ hybrids have the largest photocurrent and a

periodic on/off response compared to the photocurrent generated by reference samples (Fig. S19a), demonstrating that $\text{Ni}/\text{H}_x\text{WO}_{3-y}$ hybrids have the highest photogenerated carrier separation efficiency. The Nyquist plots of the electrochemical impedance spectra (EIS; Fig. S19b) show that $\text{Ni}/\text{H}_x\text{WO}_{3-y}$ hybrids display an obviously smaller semicircle diameter than reference samples, indicating a smaller resistance and an increased charge transfer capacity of $\text{Ni}/\text{H}_x\text{WO}_{3-y}$ hybrids. Moreover, compared to reference samples, $\text{Ni}/\text{H}_x\text{WO}_{3-y}$ hybrids show a weaker band-to-band emission peak at 580 nm in the photoluminescence (PL) spectra (Fig. S19c) owing to the suppression of radiative recombination pathway for the photogenerated carriers [51]. Furthermore, we obtain carrier lifetime by analyzing time-resolved PL (TRPL) spectra (Fig. S19d) to derive charge-transfer kinetics. $\text{Ni}/\text{H}_x\text{WO}_{3-y}$ hybrids have a longer τ (0.10 ns) than WO_3 (0.08 ns), which reflects that photogenerated electrons tend to concentrate in the dual active sites for NH_3 synthesis rather

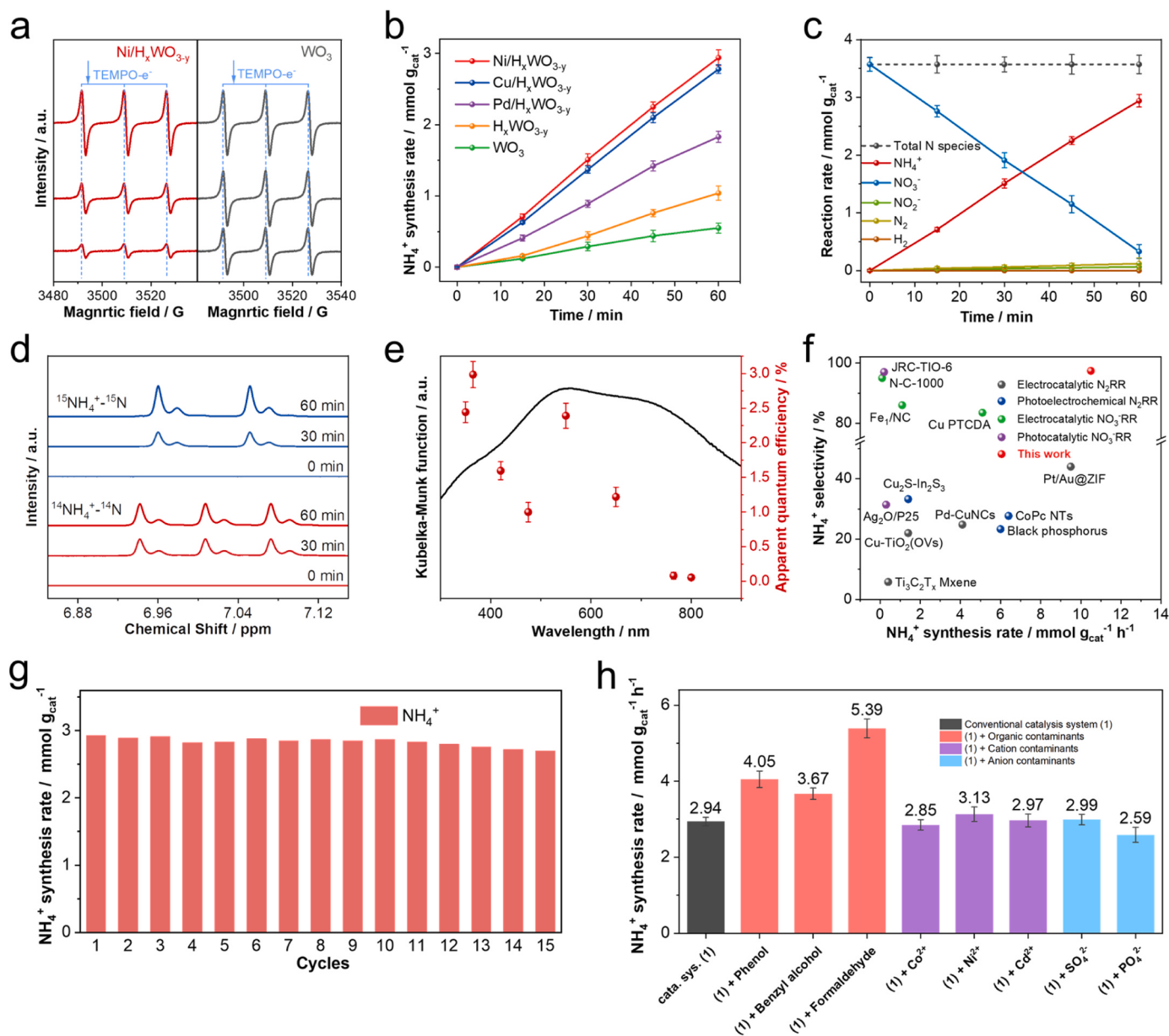


Fig. 3. (a) EPR spectra for TEMPO showing the reactive species of $\text{Ni}/\text{H}_x\text{WO}_{3-y}$ hybrids and WO_3 . (b) Time-dependent concentration change of NH_4^+ . (c) Time-dependent concentration change of NO_3^- , NO_2^- , NH_4^+ , N_2 , and H_2 over $\text{Ni}/\text{H}_x\text{WO}_{3-y}$ hybrids. (d) ¹H NMR spectra of time-dependent concentration change of NH_4^+ using ¹⁵NO₃ and ¹⁴NO₃ as the NO₃ source. (e) AQEs (red spots) of NO_3^- reduction under monochromatic light irradiation are calculated against UV/Vis-NIR absorption spectrum. (f) Comparison of the selectivity and rates of NH_4^+ synthesis through different methods under ambient conditions [52-62]. (g) Cycle test of photocatalytic NH_4^+ synthesis by NO_3^- reduction on $\text{Ni}/\text{H}_x\text{WO}_{3-y}$ hybrids. (h) NH_4^+ synthesis rates after the addition of different pollutants (organic, cationic, and anionic pollutants).

than recombine with holes. To verify the ability for generating active radicals on $\text{Ni}/\text{H}_x\text{WO}_{3-y}$ hybrids, we perform EPR experiments utilizing 2,2,6,6-tetramethyl-1-piperidinyloxy (TEMPO) as the trapping reagent (Fig. 3a and Fig. S20). The TEMPO signals on $\text{Ni}/\text{H}_x\text{WO}_{3-y}$ hybrids diminish rapidly under light irradiation compared to that on pristine WO_3 , indicating that more photoexcited electrons can be produced and consumed over $\text{Ni}/\text{H}_x\text{WO}_{3-y}$ hybrids. Additionally, the signals of another trapping agent 5,5-dimethyl-1-pyrroline N-oxide (DMPO) in light irradiation are much stronger than those in dark (Fig. S21), suggesting that $\text{Ni}/\text{H}_x\text{WO}_{3-y}$ hybrids can produce more O_2^\bullet and •OH compared to reference samples. Meanwhile, for $\text{Ni}/\text{H}_x\text{WO}_{3-y}$ hybrids, the quantities of the generated O_2^\bullet and •OH under visible light irradiation are obviously stronger than those in dark condition. In conclusion, the introductions of OVs and Ni SAs in $\text{Ni}/\text{H}_x\text{WO}_{3-y}$ hybrids greatly enhance the separation efficiency of photogenerated electron-hole pairs. According to $(ahv)^2$ versus (hv) (Fig. S22a), the calculated bandgap of $\text{Ni}/\text{H}_x\text{WO}_{3-y}$ hybrids is 1.28 eV, which is significantly less than the bandgaps of WO_3 (2.57 eV), Ni/WO_3 (2.50 eV), and $\text{H}_x\text{WO}_{3-y}$ (1.66 eV). Mott-Schottky measurement (Fig. S22b) is conducted from the electrochemical approach to determine the position of the flat band potential. All photocatalysts have positive slope, which is characteristic of n-type semiconductors. $\text{Ni}/\text{H}_x\text{WO}_{3-y}$ hybrids show the lowest flat band potential (Fermi level, E_F), corresponding to the lowest surface work function. This enables efficient transfer of electrons from $\text{H}_x\text{WO}_{3-y}$ to Ni SAs. Furthermore, based on the valence band XPS (VB-XPS) spectra (Fig. S22c), VBs of WO_3 and $\text{Ni}/\text{H}_x\text{WO}_{3-y}$ hybrids are estimated to be 2.70 and 2.45 eV, respectively. Notably, VB spectrum of $\text{Ni}/\text{H}_x\text{WO}_{3-y}$ hybrids clearly shows the existence of a defect band, which is derived from local electron induction in the d orbitals of W^{5+} species. Based on the electronic band structures vs vacuum level (Fig. S22d) [23], the conduction band position of $\text{Ni}/\text{H}_x\text{WO}_{3-y}$ hybrids is much lower than E_F due to the presence of defect bands, representing the characteristic of $\text{Ni}/\text{H}_x\text{WO}_{3-y}$ hybrids with degenerate semiconductors.

3.4. Photocatalytic performance of NH_3 synthesis from NO_3^-

After obtaining the configuration of OVs and Ni SAs, we further explore the performance of $\text{Ni}/\text{H}_x\text{WO}_{3-y}$ hybrids in photocatalytic NO_3^- reduction to NH_3 ($\text{NO}_3^- + 8\text{e}^- + 9\text{H}^+ \rightarrow \text{NH}_3 + 3\text{H}_2\text{O}$) at ambient conditions, which is conducted in 50 mL of KNO_3 solution (10 mg/L of NO_3^-) with 10.0 % ethylene glycol (EG) as the hole sacrificial agent under full spectrum illumination. The presence of EG has no effect on the quantitative detection of NH_4^+ using Nessler's reagent (Fig. S23), ^1H NMR spectra (Fig. S24), and cation chromatography (Fig. S25). As shown in Fig. 3b, small amounts of NH_4^+ are generated on commercial WO_3 (0.55 mmol $\text{g}_{\text{cat}}^{-1} \text{h}^{-1}$). The efficiency of NH_3 synthesis on $\text{H}_x\text{WO}_{3-y}$ with OVs is initially improved (1.04 mmol $\text{g}_{\text{cat}}^{-1} \text{h}^{-1}$). Notably, the simultaneous introduction of OVs and SAs (i.e., $\text{Ni}/\text{H}_x\text{WO}_{3-y}$, $\text{Cu}/\text{H}_x\text{WO}_{3-y}$, and $\text{Pd}/\text{H}_x\text{WO}_{3-y}$) can dramatically improve the activity of NH_3 synthesis. Among them, $\text{Ni}/\text{H}_x\text{WO}_{3-y}$ hybrids achieve the highest NH_3 yield of 2.94 mmol $\text{g}_{\text{cat}}^{-1} \text{h}^{-1}$, which is 2.82, 2.67, and 5.35 times higher than that of $\text{H}_x\text{WO}_{3-y}$, Ni/WO_3 (Fig. S26), and WO_3 , respectively, highlighting the important role of OVs and SAs. Specifically, with the increase of reaction time, NH_4^+ yield rate increases and reaches the maximum after 60 min (Fig. 3c) with NH_4^+ synthesis selectivity of 98.26 %, while the concentration of NO_3^- gradually decreases. Moreover, few by-products (NO_2 , N_2 , and H_2) are produced, confirming that NO_3^- is mainly converted to NH_4^+ in photocatalytic NO_3^- reduction to NH_3 . Meanwhile, the amount of total nitrogen in the reaction mixture remains stable and the trace production of by-products indicates that the five-electron-transfer synthesis of nitrogen and the water-cracking side reaction are effectively suppressed. Furthermore, to eliminate the potential effects of other nitrogen-containing substances, we conduct blank control group experiments in the absence of catalyst and NO_3^- (Fig. S27), which indicate that no NH_4^+ is generated. Moreover, ^{15}N and ^{14}N isotopic labeling experiments are also performed, where NO_3^- and the produced

NH_4^+ are detected by IC (Fig. S28) and ^1H NMR (Fig. 3d and Fig. S29) technologies. K^{14}NO_3 and K^{15}NO_3 solutions are used as N sources. The ^1H NMR spectra of the reaction solution after photocatalytic reduction of K^{15}NO_3 show a clear double peak typical of $^{15}\text{NH}_4^+$ (7.05 and 6.96 ppm) and no triple peak typical of $^{14}\text{NH}_4^+$ (7.07, 7.01, and 6.94 ppm). Both $^{15}\text{NH}_4^+$ and $^{14}\text{NH}_4^+$ are quantified by comparing the peak areas of external standards (maleic acid, $\text{C}_4\text{H}_4\text{O}_4$; Fig. S29). Based on the similar rates for $^{14}\text{NO}_3^-/^{15}\text{NO}_3^-$ reduction and $^{14}\text{NH}_4^+/^{15}\text{NH}_4^+$ production (Fig. 3d and Fig. S28), the generated NH_4^+ is confirmed to be directly sourced from NO_3^- feedstock rather than other N-containing species. The apparent quantum efficiencies (AQEs) of $\text{Ni}/\text{H}_x\text{WO}_{3-y}$ hybrids are evaluated under different monochromatic light irradiation (Fig. 3e) to investigate light utilization efficiency. The AQEs show essentially the same optical absorption trends in the visible and near-infrared regions as the $\text{Ni}/\text{H}_x\text{WO}_{3-y}$ hybrids. It can be seen that the AQE reaches 2.39 % at 550 nm, which indicates that the excitation of $\text{H}_x\text{WO}_{3-y}$ mainly comes from LSPRs effect induced by OVs in the $\text{Ni}/\text{H}_x\text{WO}_{3-y}$ hybrids.

As the reaction parameters directly affect the catalytic efficiency, an in-depth modification of the NO_3^- concentration and catalyst dosage are performed to further enhance the catalytic performance. The best reaction kinetics of NH_3 synthesis achieve in NO_3^- concentration of 60.0 mg/L (Fig. S30) and the catalyst dosage of 1.0 mg (Fig. S31). Ultimately, the optimized reaction conditions resulted in a photosynthesis rate of 10.5 mmol $\text{g}_{\text{cat}}^{-1} \text{h}^{-1}$ for NH_4^+ over $\text{Ni}/\text{H}_x\text{WO}_{3-y}$ hybrids. More importantly, compared to other NH_3 synthesis pathways under ambient conditions (Fig. 3f), the NH_3 yield and selectivity by photocatalytic NO_3^- reduction on $\text{Ni}/\text{H}_x\text{WO}_{3-y}$ hybrids are still in a relatively leading position among photocatalytic NH_3 synthesis fields, even surpassing some electrocatalytic NH_3 synthesis work despite the fact that electrocatalytic process delivers a much higher input power[52–65]. In addition, the stability of $\text{Ni}/\text{H}_x\text{WO}_{3-y}$ hybrids is further investigated (Fig. 3g). The activity of NH_3 synthesis only shows a slightly downward trend during 15 cycle tests, confirming the photostability of $\text{Ni}/\text{H}_x\text{WO}_{3-y}$ hybrids. Moreover, the XRD, Raman, XPS, and UV-vis spectra (Fig. S32) after reaction remain almost unchanged, also confirming its application stability.

Considering that the real wastewater not only contains NO_3^- but also contains various organic pollutants, they can also be served as pore sacrificial agents in the photocatalytic process. To simulated wastewater, we add phenol, benzyl alcohol, and formaldehyde as potential contaminants in photocatalysis system (Fig. 3h). We find that NH_3 yield rate has no decrease in simulated wastewater, indicating the potential of $\text{Ni}/\text{H}_x\text{WO}_{3-y}$ hybrids in actual organic wastewater. Meanwhile, cation (Co^{2+} , Ni^{2+} , and Cd^{2+}) and anion (SO_4^{2-} and PO_4^{3-}) contaminants in real wastewater have few effects on the stability of $\text{Ni}/\text{H}_x\text{WO}_{3-y}$ hybrids. It demonstrates that $\text{Ni}/\text{H}_x\text{WO}_{3-y}$ hybrids with Ni SAs and OVs have significant scientific implications in the field of environmental remediation and energy conversion.

3.5. Proposed mechanism and DFT calculations

Based on the key roles of OVs and Ni SAs of $\text{Ni}/\text{H}_x\text{WO}_{3-y}$ hybrids, we further perform in situ EPR to verify the active sites of $\text{Ni}/\text{H}_x\text{WO}_{3-y}$ hybrids in photocatalytic NO_3^- reduction to NH_3 . Firstly, in the time-dependent in situ EPR spectroscopy measurements (Fig. 4a), comparing the EPR spectrum of $\text{H}_x\text{WO}_{3-y}$ (Fig. S33), the peak at $g = 2.003$ can be assigned to the OVs, while the signals at $g_{\parallel} = 2.25$ and $g_{\perp} = 2.07$ indicate the formation of $\text{Ni}(\text{I})$ species in $\text{Ni}/\text{H}_x\text{WO}_{3-y}$ hybrids [66]. The normalized intensities of OVs and $\text{Ni}(\text{I})$ are further computed to clearly depict the dynamics of each site (Fig. S34). Interestingly, the normalized intensity of OVs gradually increases after irradiation, while the normalized intensity of $\text{Ni}(\text{I})$ decreases after enrichment of electrons to $\text{Ni} (0)$. They gradually reach the equilibrium intensity after 10 min [67]. Finally, the normalized intensities of OVs and $\text{Ni}(\text{I})$ almost return to the initial levels in 6 min after turning off the light, demonstrating both OVs and Ni SAs of $\text{Ni}/\text{H}_x\text{WO}_{3-y}$ hybrids are the dual active sites in

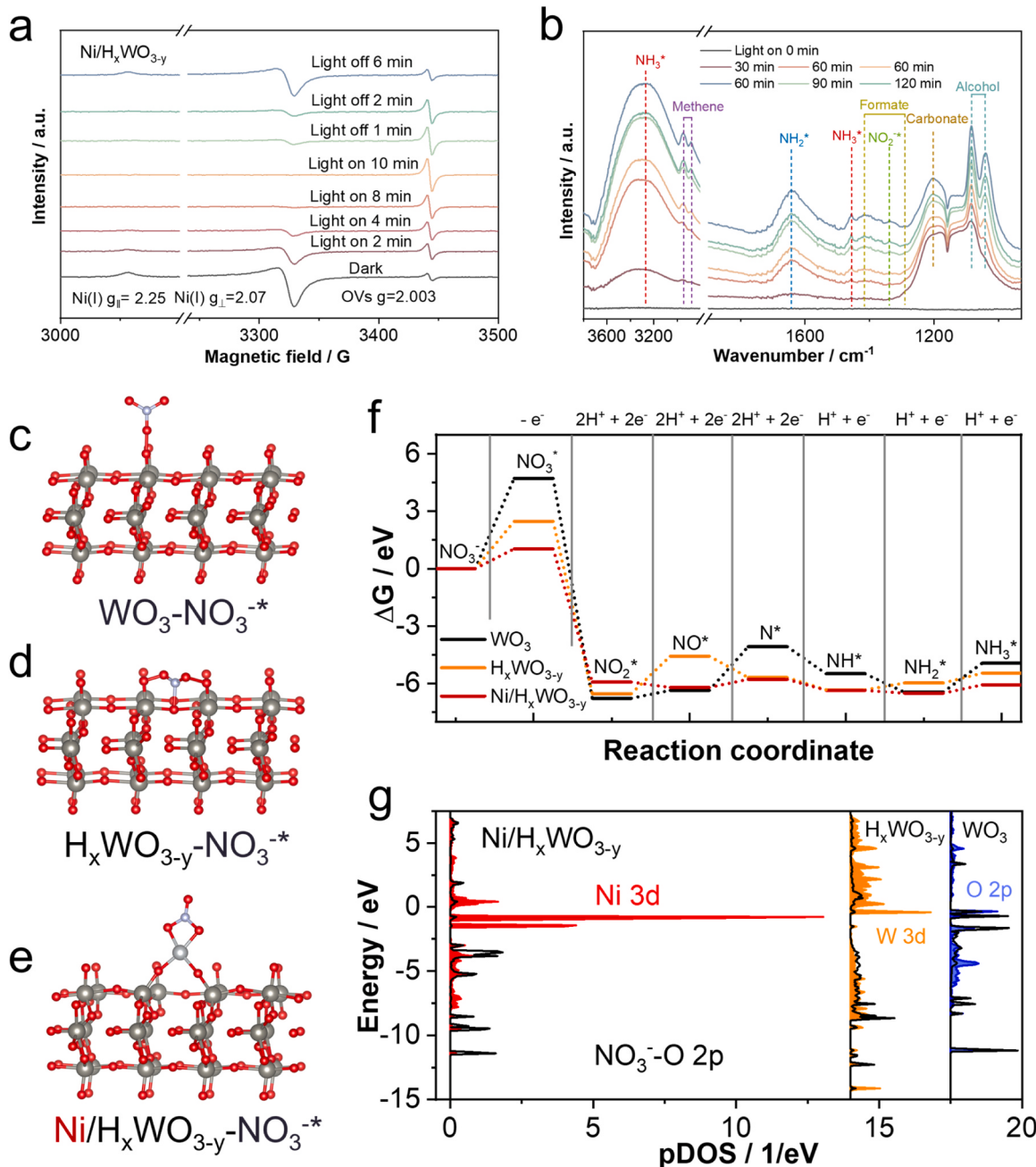


Fig. 4. (a) In situ EPR spectra at 77 K (cooled by liquid nitrogen), and (b) in situ DRIFTS in photocatalytic NO_3^- reduction to NH_3 over $\text{Ni}/\text{H}_x\text{WO}_{3-y}$ hybrids. Adsorption models of NO_3^* on (c) O-WO_3 , (d) OV site of $\text{H}_x\text{WO}_{3-y}$, and (e) Ni site of $\text{Ni}/\text{H}_x\text{WO}_{3-y}$ hybrids, respectively. (f) Free-energy diagram for photocatalytic NO_3^- reduction to NH_3 over $\text{Ni}/\text{H}_x\text{WO}_{3-y}$ hybrids. (g) pDOS plots of NO_3^* adsorption on $\text{Ni}/\text{H}_x\text{WO}_{3-y}$, $\text{H}_x\text{WO}_{3-y}$, and WO_3 .

photocatalytic NO_3^- reduction to NH_3 . Based on the above analysis, we can conclude that photogenerated electrons of $\text{H}_x\text{WO}_{3-y}$ are successfully trapped by OVs and Ni SAs in light irradiation and the initial state is restored after turning off the light. Thus, $\text{Ni}/\text{H}_x\text{WO}_{3-y}$ hybrids cannot be easily corroded in NO_3^- reduction under light irradiation. Moreover, in situ diffused reflectance infrared Fourier transform spectroscopy (DRIFTS) technique is performed to detect the key molecular intermediates and clarify the reaction mechanism (Fig. 4b). The positive peaks at 1339 cm^{-1} are attributed to NO_2^* intermediates, while the peaks at 1646 cm^{-1} are assigned to NH_2^* . It is evident that the peak intensities of NH_4^* (3270 and 1453 cm^{-1}) rise with the increase of reaction time, which is consistent with the reaction path of NH_3 synthesis by NO_3^- reduction. Meanwhile, the EG in the effluent actually acts as a pore sacrificial agent in the catalytic system, thus, the pathway of

EG-catalyzed oxidation is also explored by DRIFTS technique. With increasing reaction time, we can observe the formation and accumulation of methane (2948 and 2877 cm^{-1}), alcohol (1085 and 1040 cm^{-1}), formate (1418 and 1291 cm^{-1}), and carbonate (1203 cm^{-1}), which can be attributed to the EG catalytic oxidation. Based on the detection of reaction process by in situ DRIFTS, we deduce pathways for NO_3^- reduction to NH_3 including the transfer of eight electrons and nine protons ($\text{NO}_3^- + 8\text{e}^- + 9\text{H}^+ \rightarrow \text{NH}_3 + 3\text{H}_2\text{O}$).

To prove the above conclusion, we further calculate the relative free energies of the intermediates on $\text{Ni}/\text{H}_x\text{WO}_{3-y}$ hybrids and reference samples in NO_3^- reduction to NH_3 by DFT calculations with the assistance of computational hydrogen electrode model [68]. The stable structural configurations of WO_3 , $\text{H}_x\text{WO}_{3-y}$, and $\text{Ni}/\text{H}_x\text{WO}_{3-y}$ hybrids are shown in Fig. 4c-e. When OVs are introduced to WO_3 , the adsorption site of

NO_3^- transfers from O atom of WO_3 to OVs of $\text{H}_x\text{WO}_{3-y}$. For $\text{Ni}/\text{H}_x\text{WO}_{3-y}$ hybrids, Ni SAs are the adsorption site of NO_3^- . The adsorption energies of NO_3^- on Ni SA-Ni/ $\text{H}_x\text{WO}_{3-y}$ hybrids (1.28 eV) and OV- $\text{H}_x\text{WO}_{3-y}$ (2.47 eV) are significantly lower than those on O- WO_3 (4.72 eV), indicating that the dual active sites in $\text{Ni}/\text{H}_x\text{WO}_{3-y}$ hybrids are more favorable for NO_3^- adsorption (Fig. 4f). Notably, $\text{Ni}/\text{H}_x\text{WO}_{3-y}$ hybrids greatly reduce the energy of the rate-determining steps for $\text{H}_x\text{WO}_{3-y}$ ($\text{NO}_2^* \rightarrow \text{NO}^*$), suggesting that Ni SAs can kinetically accelerate the deoxygenation process. In addition, the projected density of states (pDOS) between the electron orbitals of the different adsorption sites and the 2p orbitals of NO_3^- -O (Fig. 4g) is used to probe the electronic band structure. By comparing the overlap between the Ni 3d- O 2p, W 3d - O 2p, and O 2p - O 2p, the p-d orbital hybridizations of OVs and Ni SAs dual active sites and NO_3^* are obviously stronger than that of WO_3 . Therefore, electrons can be easily transferred to the coordination O of NO_3^* through the Ni-O and W-O bonds. Moreover, OVs and Ni SAs significantly increase the density of states near the E_F level, which facilitates the electron conductivity and electron transfer ability[69].

4. Conclusion

In summary, we prepare $\text{Ni}/\text{H}_x\text{WO}_{3-y}$ hybrids containing abundant OVs and Ni SAs to efficiently and highly selective reduce NO_3^- to NH_3 by photocatalysis. $\text{Ni}/\text{H}_x\text{WO}_{3-y}$ hybrids have highly selective and efficient photocatalytic NH_3 synthesis from NO_3^- reduction. The synergistic effect of OVs and Ni SAs plays a key role in NH_3 synthesis, that is, (1) OVs act as adsorption sites of NO_3^- and transfer photogenerated electron and adsorbed NO_3^- to Ni SAs by LSPRs effect; (2) Ni SAs are mainly responsible for NO_3^- reduction to NH_3 . Meanwhile, the strong hybridization of 3d-2p orbitals between Ni SAs and NO_3^- -O further promotes the electrons transfer from Ni SAs to NO_3^- . And the induction of Ni SAs effectively reduce the free energy of the rate-limiting step ($\text{NO}_2^* \rightarrow \text{NO}^*$) of $\text{H}_x\text{WO}_{3-y}$. This study provides a promising strategy for exploring metal SAs/plasmonic semiconductor with dual active sites for the pollutants treatment in wastewater.

CRediT authorship contribution statement

Yunlong Wang, Haibo Yin, and Xiaoguang Zhao contributed equally to this work. Yunlong Wang, Haibo Yin, and Xiaoguang Zhao proposed, designed and performed the experiments, and analyzed data. All authors discussed, commented on and revised the manuscript.

Declaration of Competing Interest

The authors declare no competing financial interest.

Data availability

Data will be made available on request.

Acknowledgments

This work was financially supported by National Natural Science Foundation of China (22206096) and China Petrochemical Corporation funding (Sinopec Group, no. 323032). This work was also financially supported by China Postdoctoral Science Foundation (2020TQ0166 and 2021M691771).

Appendix A. Supporting information

Supplementary data associated with this article can be found in the online version at [doi:10.1016/j.apcatb.2023.123266](https://doi.org/10.1016/j.apcatb.2023.123266).

References

- P.H. van Langevelde, I. Katsounaros, M.T.M. Koper, Electrocatalytic nitrate reduction for sustainable ammonia production, Joule 5 (2021) 290–294.
- Q. Wang, J. Pan, J. Guo, H.A. Hansen, H. Xie, L. Jiang, L. Hua, H. Li, Y. Guan, P. Wang, W. Gao, L. Liu, H. Cao, Z. Xiong, T. Vegge, P. Chen, Ternary ruthenium complex hydrides for ammonia synthesis via the associative mechanism, Nat. Catal. 4 (2021) 959–967.
- Y. Wang, W. Zhou, R. Jia, Y. Yu, B. Zhang, Unveiling the activity origin of a copper-based electrocatalyst for selective nitrate reduction to ammonia, Angew. Chem. Int. Ed. Engl. 59 (2020) 5350–5354.
- N.C. Kani, J.A. Gauthier, A. Prajapati, J. Edgington, I. Bordawekar, W. Shields, M. Shields, L.C. Seitz, A.R. Singh, M.R. Singh, Solar-driven electrochemical synthesis of ammonia using nitrate with 11% solar-to-fuel efficiency at ambient conditions, Energy Environ. Sci. 14 (2021) 6349–6359.
- M. Wang, M.A. Khan, I. Mohsin, J. Wicks, A.H. Ip, K.Z. Sumon, C.-T. Dinh, E. H. Sargent, I.D. Gates, M.G. Kibria, Can sustainable ammonia synthesis pathways compete with fossil-fuel based Haber–Bosch processes? Energy Environ. Sci. 14 (2021) 2535–2548.
- Y. Wang, C. Wang, M. Li, Y. Yu, B. Zhang, Nitrate electroreduction: mechanism insight, in situ characterization, performance evaluation, and challenges, Chem. Soc. Rev. 50 (2021) 6720–6733.
- A.P. Murphy, Chemical removal of nitrate from water, Nature 350 (1991) 223–225.
- H. Xu, Y. Ma, J. Chen, W.-x Zhang, J. Yang, Electrocatalytic reduction of nitrate – a step towards a sustainable nitrogen cycle, Chem. Soc. Rev. 51 (2022) 2710–2758.
- J. Li, R. Chen, J. Wang, Y. Zhou, G. Yang, F. Dong, Subnanometric alkaline-earth oxide clusters for sustainable nitrate to ammonia photosynthesis, Nat. Commun. 13 (2022) 1098.
- K.-H. Kim, H. Lee, X. Huang, J.H. Choi, C. Chen, J.K. Kang, D. O'Hare, Energy-efficient electrochemical ammonia production from dilute nitrate solution, Energy Environ. Sci. 16 (2023) 663–672.
- P.J. Chirik, One electron at a time, Nat. Chem. 1 (2009) 520–522.
- K.E.C. Smith, Y. Jeong, Passive sampling and dosing of aquatic organic contaminant mixtures for ecotoxicological analyses, Environ. Sci. Technol. 55 (2021) 9538–9547.
- H. Yin, Z. Chen, S. Xiong, J. Chen, C. Wang, R. Wang, Y. Kuwahara, J. Luo, H. Yamashita, Y. Peng, J. Li, Alloying effect-induced electron polarization drives nitrate electroreduction to ammonia, Chem. Catal. 1 (2021) 1088–1103.
- Y. Wang, J. Hu, T. Ge, F. Chen, Y. Lu, R. Chen, H. Zhang, B. Ye, S. Wang, Y. Zhang, T. Ma, H. Huang, Gradient cationic vacancies enabling inner-to-outer tandem homojunction: strong local internal electric field and reformed basic sites boosting CO_2 photoreduction, Adv. Mater. (2023), 2302538.
- X. Zheng, L. Feng, Y. Dou, H. Guo, Y. Liang, G. Li, J. He, P. Liu, J. He, High carrier separation efficiency in morphology-controlled BiOBr/C Schottky junctions for photocatalytic overall water splitting, ACS Nano 15 (2021) 13209–13219.
- X. Zhang, P. Ma, C. Wang, L. Gan, X. Chen, P. Zhang, Y. Wang, H. Li, L. Wang, X. Zhou, K. Zheng, Unraveling the dual defect sites in graphite carbon nitride for ultra-high photocatalytic H_2O_2 evolution, Energy Environ. Sci. 15 (2022) 830–842.
- J. Wu, Y. Huang, W. Ye, Y. Li, CO_2 reduction: from the electrochemical to photochemical approach, Adv. Sci. 4 (2017), 1700194.
- Y. Zhao, W. Gao, S. Li, G.R. Williams, A.H. Mahadi, D. Ma, Solar- versus thermal-driven catalysis for energy conversion, Joule 3 (2019) 920–937.
- H. Yin, J. Li, New insight into photocatalytic CO_2 conversion with nearly 100% CO selectivity by $\text{CuO-Pd}/\text{H}_x\text{MoO}_{3-y}$ hybrids, Appl. Catal. B 320 (2023), 121927.
- M.A. Rahman, S. Bazargan, S. Srivastava, X. Wang, M. Abd-Elhalla, J.P. Thomas, N. F. Heinig, D. Pradhan, K.T. Leung, Defect-rich decorated TiO_2 nanowires for super-efficient photoelectrochemical water splitting driven by visible light, Energy Environ. Sci. 8 (2015) 3363–3373.
- P. Xia, X. Pan, S. Jiang, J. Yu, B. He, P.M. Ismail, W. Bai, J. Yang, L. Yang, H. Zhang, M. Cheng, H. Li, Q. Zhang, C. Xiao, Y. Xie, Designing a redox heterojunction for photocatalytic “overall nitrogen fixation” under mild conditions, Adv. Mater. 34 (2022), 2200563.
- H. Yin, Z. Chen, Y. Peng, S. Xiong, Y. Li, H. Yamashita, J. Li, Dual active centers bridged by oxygen vacancies of ruthenium single-atom hybrids supported on molybdenum oxide for photocatalytic ammonia synthesis, Angew. Chem. Int. Ed. Engl. 61 (2022), e202114242.
- L. Liang, X. Li, Y. Sun, Y. Tan, X. Jiao, H. Ju, Z. Qi, J. Zhu, Y. Xie, Infrared light-driven CO_2 overall splitting at room temperature, Joule 2 (2018) 1004–1016.
- J. Xu, H. Xu, A. Dong, H. Zhang, Y. Zhou, H. Dong, B. Tang, Y. Liu, L. Zhang, X. Liu, J. Luo, J. Luo, L. Bie, S. Dai, Y. Wang, X. Sun, Y. Li, Strong electronic metal-support interaction between iridium single atoms and a WO_3 support promotes highly efficient and robust CO_2 cycloaddition, Adv. Mater 34 (2022) 2206991.
- H. Cheng, T. Kamegawa, K. Mori, H. Yamashita, Surfactant-free nonaqueous synthesis of plasmonic molybdenum oxide nanosheets with enhanced catalytic activity for hydrogen generation from ammonia borane under visible light, Angew. Chem. Int. Ed. Engl. 53 (2014) 2910–2914.
- S. Sun, M. Watanabe, J. Wu, Q. An, T. Ishihara, Ultrathin $\text{WO}_3(0.33\text{H}(2))$ nanotubes for $\text{CO}(2)$ photoreduction to acetate with high selectivity, J. Am. Chem. Soc. 140 (2018) 6474–6482.
- H. Yin, Y. Peng, J. Li, Electrocatalytic reduction of nitrate to ammonia via a Au/Cu single atom alloy catalyst, Environ. Sci. Technol. 57 (2023) 3134–3144.
- H. Yin, F. Dong, D. Wang, J. Li, Coupling Cu single atoms and phase junction for photocatalytic CO_2 reduction with 100% CO selectivity, ACS Catal. 12 (2022) 14096–14105.
- Z.-H. Xue, D. Luan, H. Zhang, X.W. Lou, Single-atom catalysts for photocatalytic energy conversion, Joule 6 (2022) 92–133.

[30] H. Liu, S. Yang, G. Wang, H. Liu, Y. Peng, C. Sun, J. Li, J. Chen, Strong electronic orbit coupling between cobalt and single-atom praseodymium for boosted nitrous oxide decomposition on Co₃O₄ catalyst, *Environ. Sci. Technol.* 56 (2022) 16325–16335.

[31] X.F. Cheng, J.H. He, H.Q. Ji, H.Y. Zhang, Q. Cao, W.J. Sun, C.L. Yan, J.M. Lu, Coordination symmetry breaking of single-atom catalysts for robust and efficient nitrate electroreduction to ammonia, *Adv. Mater.* 34 (2022), e2205767.

[32] Z.Y. Wu, M. Karamad, X. Yong, Q. Huang, D.A. Cullen, P. Zhu, C. Xia, Q. Xiao, M. Shakouri, F.-Y. Chen, J.Y. Kim, Y. Xia, K. Heck, Y. Hu, M.S. Wong, Q. Li, I. Gates, S. Siahrostami, H. Wang, Electrochemical ammonia synthesis via nitrate reduction on Fe single atom catalyst, *Nat. Commun.* 12 (2021) 2870.

[33] Y. Yang, Y.M. Qian, H.J. Li, Z.H. Zhang, Y.W. Mu, D. Do, B. Zhou, J. Dong, W. J. Yan, Y. Qin, L. Fang, R.F. Feng, J.G. Zhou, P. Zhang, J.C. Dong, G.H. Yu, Y.Y. Liu, X.M. Zhang, X.J. Fan, O-coordinated W-Mo dual-atom catalyst for pH-universal electrocatalytic hydrogen evolution, *Sci. Adv.* 6 (2020).

[34] M. Gong, W. Zhou, M.C. Tsai, J. Zhou, M. Guan, M.C. Lin, B. Zhang, Y. Hu, D. Y. Wang, J. Yang, S.J. Pennycook, B.J. Hwang, H. Dai, Nanoscale nickel oxide/nickel heterostructures for active hydrogen evolution electrocatalysis, *Nat. Commun.* 5 (2014) 4695–4701.

[35] L. Li, C. Tang, X. Cui, Y. Zheng, X. Wang, H. Xu, S. Zhang, T. Shao, K. Davey, S. Qiao, Efficient nitrogen fixation to ammonia through integration of plasma oxidation with electrocatalytic reduction, *Angew. Chem. Int. Ed. Engl.* 60 (2021) 14131–14137.

[36] Y. Wang, A. Xu, Z. Wang, L. Huang, J. Li, F. Li, J. Wicks, M. Luo, D.H. Nam, C. S. Tan, Y. Ding, J. Wu, Y. Lum, C.T. Dinh, D. Sinton, G. Zheng, E.H. Sargent, Enhanced nitrate-to-ammonia activity on copper-nickel alloys via tuning of intermediate adsorption, *J. Am. Chem. Soc.* 142 (2020) 5702–5708.

[37] G. Wang, Y. Ling, H. Wang, X. Yang, C. Wang, J.Z. Zhang, Y. Li, Hydrogen-treated WO₃ nanoflakes show enhanced photostability, *Energy Environ. Sci.* 5 (2012).

[38] J. Cai, M. Wu, Y. Wang, H. Zhang, M. Meng, Y. Tian, X. Li, J. Zhang, L. Zheng, J. Gong, Synergetic enhancement of light harvesting and charge separation over surface-disorder-engineered TiO₂ photonic, *Cryst., Chem.* 2 (2017) 877–892.

[39] J. Cai, A. Cao, J. Huang, W. Jin, J. Zhang, Z. Jiang, X. Li, Understanding oxygen vacancies in disorder-engineered surface and subsurface of CaTiO₃ nanosheets on photocatalytic hydrogen evolution, *Appl. Catal. B* 267 (2020).

[40] G. Liu, J. Han, X. Zhou, L. Huang, F. Zhang, X. Wang, C. Ding, X. Zheng, H. Han, C. Li, Enhancement of visible-light-driven O₂ evolution from water oxidation on WO₃ treated with hydrogen, *J. Catal.* 307 (2013) 148–152.

[41] X. Yao, K. Klyukin, W. Lu, M. Onen, S. Ryu, D. Kim, N. Emond, I. Waluyo, A. Hunt, J.A. Del Alamo, J. Li, B. Yıldız, Protonic solid-state electrochemical synapse for physical neural networks, *Nat. Commun.* 11 (2020) 3134.

[42] S. Ju, H.-J. Seok, J. Jun, D. Huh, S. Son, K. Kim, W. Kim, S. Baek, H.-K. Kim, H. Lee, Fully blossomed WO₃/BiVO₄ structure obtained via active facet engineering of patterned FTO for highly efficient Water splitting, *Appl. Catal. B* 263 (2020).

[43] Y. Lee, G. He, A.J. Akey, R. Si, M. Flytzani-Stephanopoulos, I.P. Herman, Raman analysis of mode softening in nanoparticle CeO₂(δ) and Au-CeO₂(δ) during CO oxidation, *J. Am. Chem. Soc.* 133 (2011) 12952–12955.

[44] X. Liang, L. Yan, W. Li, Y. Bai, C. Zhu, Y. Qiang, B. Xiong, B. Xiang, X. Zou, Flexible high-energy and stable rechargeable vanadium-zinc battery based on oxygen defect modulated V₂O₅ cathode, *Nano Energy* 87 (2021).

[45] A. Tocchetto, A. Glisenti, Study of the interaction between simple molecules and W–Sn based oxide catalysts, *Langmuir* 16 (2000) 2642–2650.

[46] H. Khan, M.G. Rigamonti, D.C. Boffito, Enhanced photocatalytic activity of Pt-TiO₂/WO₃ hybrid material with energy storage ability, *Appl. Catal. B* 252 (2019) 77–85.

[47] Z. Chen, J. Wang, G. Zhai, W. An, Y. Men, Hierarchical yolk-shell WO₃ microspheres with highly enhanced photoactivity for selective alcohol oxidations, *Appl. Catal. B* 218 (2017) 825–832.

[48] J. Zhou, X. An, Q. Tang, H. Lan, Q. Chen, H. Liu, J. Qu, Dual channel construction of WO₃ photocatalysts by solution plasma for the persulfate-enhanced photodegradation of bisphenol A, *Appl. Catal. B* 277 (2020).

[49] J. Yan, L. Kong, Y. Ji, J. White, Y. Li, J. Zhang, P. An, S. Liu, S.-T. Lee, T. Ma, Single atom tungsten doped ultrathin α -Ni(OH)₂ for enhanced electrocatalytic water oxidation, *Nat. Commun.* 10 (2019) 2149.

[50] Y. Liu, H. Cheng, M. Lyu, S. Fan, Q. Liu, W. Zhang, Y. Zhi, C. Wang, C. Xiao, S. Wei, B. Ye, Y. Xie, Low overpotential in vacancy-rich ultrathin CoSe₂ nanosheets for water oxidation, *J. Am. Chem. Soc.* 136 (2014) 15670–15675.

[51] H. Dong, C. Zhang, W. Nie, S. Duan, C.N. Saggau, M. Tang, M. Zhu, Y.S. Zhao, L. Ma, O.G. Schmidt, Interfacial chemistry triggers ultrafast radiative recombination in metal halide perovskites, *Angew. Chem. Int. Ed. Engl.* 61 (2022), e202115875.

[52] H.-T. Ren, S.-Y. Jia, J.-J. Zou, S.-H. Wu, X. Han, A facile preparation of Ag₂O/P25 photocatalyst for selective reduction of nitrate, *Appl. Catal. B* 176–177 (2015) 53–61.

[53] D. Liu, J. Wang, S. Bian, Q. Liu, Y. Gao, X. Wang, P.K. Chu, X.F. Yu, Photoelectrochemical synthesis of ammonia with black phosphorus, *Adv. Funct. Mater.* 30 (2020).

[54] U.K. Ghorai, S. Paul, B. Ghorai, A. Adalder, S. Kapse, R. Thapa, A. Nagendra, A. Gain, Scalable production of cobalt phthalocyanine nanotubes: efficient and robust hollow electrocatalyst for ammonia synthesis at room temperature, *ACS Nano* 15 (2021) 5230–5239.

[55] K. Bi, Y. Wang, D.-M. Zhao, J.-Z. Wang, D. Bao, M.-M. Shi, Charge carrier dynamics investigation of Cu₂S-In₂S₃ heterostructures for the conversion of dinitrogen to ammonia via photo-electrocatalytic reduction, *J. Mater. Chem. A* 9 (2021) 10497–10507.

[56] G.-F. Chen, Y. Yuan, H. Jiang, S.-Y. Ren, L.-X. Ding, L. Ma, T. Wu, J. Lu, H. Wang, Electrochemical reduction of nitrate to ammonia via direct eight-electron transfer using a copper–molecular solid catalyst, *Nat. Energy* 5 (2020) 605–613.

[57] Y. Luo, G.-F. Chen, L. Ding, X. Chen, L.-X. Ding, H. Wang, Efficient electrocatalytic N₂ fixation with MXene under ambient conditions, *Joule* 3 (2019) 279–289.

[58] H. Hirakawa, M. Hashimoto, Y. Shiraishi, T. Hirai, Selective nitrate-to-ammonia transformation on surface defects of titanium dioxide photocatalysts, *ACS Catal.* 7 (2017) 3713–3720.

[59] L. Liu, T. Xiao, H. Fu, Z. Chen, X. Qu, S. Zheng, Construction and identification of highly active single-atom Fe₁-NC catalytic site for electrocatalytic nitrate reduction, *Appl. Catal. B* 323 (2023), 122181.

[60] R. Li, T. Gao, P. Wang, W. Qiu, K. Liu, Y. Liu, Z. Jin, P. Li, The origin of selective nitrate-to-ammonia electroreduction on metal-free nitrogen-doped carbon aerogel catalysts, *Appl. Catal. B* 331 (2023), 122677.

[61] H.Y.F. Sim, J.R.T. Chen, C.S.L. Koh, H.K. Lee, X. Han, G.C. Phan-Quang, J.Y. Pang, C.L. Lay, S. Pedireddy, I.Y. Phang, E.K.L. Yeow, X.Y. Ling, ZIF-Induced d-band modification in a bimetallic nanocatalyst: achieving over 44% efficiency in the ambient nitrogen reduction reaction, *Angew. Chem. Int. Ed. Engl.* 59 (2020) 16997–17003.

[62] L. Han, Z. Ren, P. Ou, H. Cheng, N. Rui, L. Lin, X. Liu, L. Zhuo, J. Song, J. Sun, J. Luo, H.L. Xin, Modulating single-atom palladium sites with copper for enhanced ambient ammonia electrosynthesis, *Angew. Chem. Int. Ed. Engl.* 60 (2021) 345–350.

[63] X. Li, P. Shen, X. Li, D. Ma, K. Chu, Sub-nm RuO_x Clusters on Pd metallene for synergistically enhanced nitrate electroreduction to ammonia, *ACS Nano* 17 (2023) 1081–1090.

[64] N. Zhang, G. Zhang, P. Shen, H. Zhang, D. Ma, K. Chu, Lewis acid Fe-V pairs promote nitrate electroreduction to ammonia, *Adv. Funct. Mater.* 33 (2023), 2211537.

[65] G. Zhang, X. Li, K. Chen, Y. Guo, D. Ma, K. Chu, Tandem electrocatalytic nitrate reduction to ammonia on MBenes, *Angew. Chem. Int. Ed. Engl.* 62 (2023), e202300054.

[66] Y. Wu, Y. Li, J. Gao, Q. Zhang, Recent advances in vacancy engineering of metal-organic frameworks and their derivatives for electrocatalysis, *SM&T* 1 (2021) 66–87.

[67] Z. Wang, J. Zhu, X. Zu, Y. Wu, S. Shang, P. Ling, P. Qiao, C. Liu, J. Hu, Y. Pan, J. Zhu, Y. Sun, Y. Xie, Selective CO₂ photoreduction to CH₄ via Pd(δ +) -assisted hydrodeoxygenation over CeO₂ nanosheets, *Angew. Chem. Int. Ed. Engl.* 61 (2022), e202203249.

[68] K. Chen, Z. Ma, X. Li, J. Kang, D. Ma, K. Chu, Single-atom Bi alloyed Pd metallene for nitrate electroreduction to ammonia, *Adv. Funct. Mater.* 33 (2023), 2209890.

[69] Y. Jiang, H. Liu, Y. Jiang, Y. Mao, W. Shen, M. Li, R. He, Adjustable heterointerface-vacancy enhancement effect in RuO₂@Co₃O₄ electrocatalysts for efficient overall water splitting, *Appl. Catal. B* 324 (2023).